/

A Spatio-Temporal Fusion Deep Learning Network with Application to Lightning Nowcasting

Changhai Zhou [a], Ling Fan[1] [b], Ferrante Neri [c,1]

[a] *Network and Information Center, Chengdu Normal University, Chengdu 611130, China*

[b] *School of Computer Science, Chengdu Normal University, Chengdu 611130, China*

[c] *Nature Inspired Computing and Engineering Research Group, School of Computer Science and Electronic Engineering, University of Surrey, Guildford, Surrey GU2 7XH, United Kingdom*

Abstract. Lightning is a rapidly evolving phenomenon, exhibiting both mesoscale and microscale characteristics. Its prediction significantly relies on timely and accurate data observation. With the implementation of new generation weather radar systems and lightning detection networks, radar reflectivity image products, and lightning observation data are becoming increasingly abundant. Research focus has shifted towards lightning nowcasting (prediction of imminent events), utilizing deep learning (DL) methods to extract lightning features from very large data sets. In this paper, we propose a novel spatio-temporal fusion deep learning lightning nowcasting network (STF-LightNet) for lightning nowcasting. The network is based on a 3-dimensional U-Net architecture with encoder-decoder blocks and adopts a structure of multiple branches as well as the main path for the encoder block. To address the challenges of feature extraction and fusion of multi-source data, multiple branches are used to extract different data features independently, and the main path fuses these features. Additionally, a spatial attention (SA) module is added to each branch and the main path to automatically identify lightning areas and enhance their features. The main path fusion is conducted in two steps: the first step fuses features from the branches, and the second fuses features from the previous and current levels of the main path using two different methods—the weighted summation fusion method and the attention gate fusion method. To overcome the sparsity of lightning observations, we employ an inverse frequency weighted cross-entropy loss function. Finally, STF-LightNet is trained using observations from the previous half hour to predict lightning in the next hour. The outcomes illustrate that the fusion of both the multi-branch and main path structures enhances the network's ability to effectively integrate features from diverse data sources. Attention mechanisms and fusion modules allow the network to capture more detailed features in the images.

Keywords. spatio-temporal fusion; deep learning; lightning nowcasting; attention gate fusion

1. Introduction

Lightning, known for its destructive impact, poses a significant threat due to the substantial economic and human losses it often incurs. Given its rapid evolution, intense weather phenomena, and small spatio-temporal scales, accurate prediction of lightning events is crucial, and the typical lead-time ranges from 0 to 2 hours [1], which is called nowcasting. Amidst concerns about global warming and the rising occurrence of extreme weather events, the significance of accurate lightning prediction is escalating [2–6].

The prevailing approach to lightning prediction involves extrapolation reliant on real-time data. This approach involves various techniques such as optical flow [7–10], TITAN [11], SCIT [12], and machine learning method [13–17], often coupled with numerical weather predictions (NWP) [10, 18] or stochastic field perturbations [10, 19]. The deployment of new generation weather radar systems and lightning observation systems has resulted in the acquisition of a massive amount of high-resolution spatio-temporal observation data. However, the extrapolation method, which heavily relies on the motion features of the observations, struggles to handle the complex non-linearities inherent in convective systems. The intricate information necessary for accurate prediction is often concealed within the vast high-resolution dataset.

[1]Corresponding Author: Ling Fan, Email: 151022@cdnu.edu.cn and Ferrante Neri, Email: f.neri@surrey.ac.uk

/

Just like in other fields [20–28], weather forecasting systems driven by spatio-temporal data and based on deep learning (DL) [29–37] have demonstrated superior performance compared to Numerical Weather Prediction (NWP) methods [38–42]. Nevertheless, these global weather forecasting models face challenges in balancing the trade-off between forecasting coverage and computational efficiency. Consequently, the resolution of these models is often limited, typically at 0.25° latitude×0.25°longitude (In geography, 0.01° is roughly equivalent to 1 kilometer). This low resolution proves to be a drawback when predicting lightning events with small spatio-temporal scales. Consequently, the majority of these models focus solely on forecasting precipitation.

Data-driven lightning forecasting/nowcasting with DL methods can be broadly categorized into two types: architectures based on recurrent neural networks (RNN) [43] and those based on convolutional neural networks (CNN) [44,45]. In the realm of RNN-based architecture, Shi et al. introduced the Convolutional Long Short-Term Memory (ConvLSTM) model in 2015. This model cleverly combines the strengths of convolutional neural networks and LSTM recurrent neural network models, demonstrating superior performance compared to traditional optical flow techniques [46]. In 2017, the same authors expanded on their work by incorporating gated recurrent units (GRUs) and introducing the convolutional gated recurrent unit (ConvGRU) and trajectory GRU (TrajGRU) algorithms [47]. Building upon Shi et al.'s foundation, Geng et al. proposed LightNet, a model that utilizes numerical models (WRF) and real-time lightning observations to predict lightning occurrences in the next 0–6 hours [48,49]. In 2022, a novel approach, Seamless Lightning Nowcasting with RNN, emerged. This method nowcasts lightning at five-minute intervals within the next hour by leveraging multi-source data, including lightning detection data, weather radar observations, satellite imagery, weather forecasts, and elevation data [50]. Later on, the Lightning Nowcasting with RNN was extended to nowcast multiple hazards [51]. In the latest research, [52] incorporated the surface feature data in addition to radar and lightning data. They extended the ConvLSTM algorithm by integrating GAN (Generative Adversarial Network) [53,54] to achieve more accurate prediction results.

The RNN structure exhibits advantages in extracting temporal features from time series, but it cannot capture spatial features. Although ConvLSTM combines CNN with RNN to address this limitation, it still falls short in terms of spatial feature extraction compared to a CNN-based structure [55]. Semantic segmentation networks, such as the U-Net, with its unique encoder-decoder structure, are recognized for achieving pixel-wise segmentation [56]. In fact, the encoder-decoder structure has been proven to be very effective in many application fields [57–60]. Notably, the U-Net incorporates skip connections from the encoder to the decoder, establishing semantic connections between encoding and decoding feature layers. This architecture allows for the simultaneous extraction of both coarse and fine image features. Viewing convective systems nowcasting as a semantic segmentation problem has led to the proposal of lightning nowcasting using semantic segmentation networks [61, 62]. Zhou et al. (2020) introduced the LightningNet method, leveraging multi-source data, including satellite cloud images, radar reflectivity, and lightning observations. They replaced the 2D convolutional layers in SegNet with a 3D convolution, treating convective systems nowcasting as a semantic segmentation task [61]. Due to the lower spatial and temporal resolution of satellite observation data compared to radar and lightning data, [61] uses linear interpolation to unify the spatial and temporal resolution of radar and lightning data with that of satellite data. However, this also results in a decrease in the spatial and temporal resolution of the lightning nowcast results. Fan et al. (2023) proposed Light3Dunet, based on the 3D U-Net architecture, which constructed a high-dimensional dataset by integrating lightning observations and radar reflectivity data. This approach aimed to enhance the accuracy of lightning nowcasting by utilizing the spatial position coupled features of Cloud-to-Ground and Intra-Cloud lightning and the 3D U-net network [62]. Both methods simplify the process by stacking multi-source data into a 3D dataset and directly extracting features using 3D convolutions, rather than independently extracting features from each data source and then fusing them. It has been demonstrated in many applications that feature selection and fusion can enhance model performance, improving predictive accuracy [63–70].

/

Based on the above analysis, this paper introduces a novel spatio-temporal fusion deep learning network for lightning nowcasting, termed STF-LightNet. The proposed method adopts a 3D U-Net architecture, featuring a multi-branch and main path configuration for the extraction and fusion of features from diverse data sources in the encoder block. To address the mesoscale and microscale characteristics of lightning, each branch incorporates a Spatial Attention (SA) module to autonomously identify and enhance the lightning region. The fusion process in the main path unfolds in two steps for extracting spatio-temporal features: first, the fusion of features from each branch, followed by the fusion of features from the current layer and the previous layer. Considering the sparsity of lightning images, a reversed frequency cross-entropy loss function is incorporated during training, assigning larger weights to less frequent grids. The proposed algorithm is then trained and evaluated using observational data from the middle of China, demonstrating its effectiveness in lightning prediction for the next hour.

The structure of the paper is organized as follows: Section 2 describes the materials used, including the architecture of the proposed model presented. The verification results are detailed in Section 3, and the conclusion is presented in Section 4.

2. Materials and Methods

2.1. Study Area

Our study area encompasses the region between 112°-117°E and 28°-33°N in the middle of China, as illustrated in Fig. 1. A S-Band weather radar, denoted by the red cross in Fig. 1, is centrally located within the study area. Operating at a 6-minute interval, the radar conducts a total of 240 scans per day. The resulting products cover a radius of 232 km with a resolution of 0.01°×0.01°, represented as a 640×480 floating-point matrix. The Lightning Detection Network servicing this area consists of 18 sensors, with only 12 shown in Fig. 1.

Subsequently, we will undertake further processing of the data acquired from the aforementioned sensors.

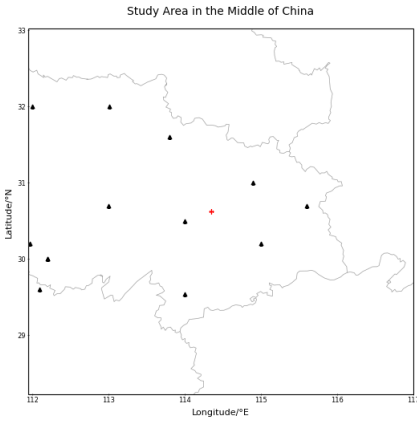

Fig. 1. The study is conducted in the middle of China, with the weather radar's location indicated by a red cross and the stations of lightning detection sensors represented by black triangles.

2.2. Data

2.2.1. Radar Data

The S-band radar depicted in Fig. 1 is part of the China Next Generation Weather Radar (CINRAD) Network. Reflectivity image products generated by the radar can be obtained from the China Meteorological Administration (CMA) website (http://data.cma.cn, accessed on November 22, 2022). We downloaded products covering two precipitation seasons (May to August) from 2018 to 2019, resulting in a total of 59,040 maps.

To address redundant information on each map, data cleaning procedures are applied, involving the removal of annotations, crack filling at the removed pixels, and cropping. The fundamental data cleaning steps align with those in [62, 71]. The reflectivity image before and after cleaning can be referred to [62]. Ultimately, each cleaned radar reflectivity image comprises 480×480 grid points, retaining only the pixel values corresponding to the colors matched with the "Reflectivity Colorbar." The "Reflectivity Colorbar" divides radar echo reflectivity intensity from 0 to 75 dBZ into 15 different colors; for more detailed illustrations, please refer to [62]. In 6 and 7 of this paper, we retained the pixel values of radar reflectivity greater than or equal to 30 dBZ and provided the corresponding colorbar. The resolution of the study area is 0.01° × 0.01°. The total number of images used in this study is 59,040, with dimensions of 480 × 480.

2.2.2. Lightning Data

The sensor network depicted in Fig. 1 is part of the National Lightning Detection Network (NLDN) in China. NLDN provided raw data products, which include the location, time, type, and other descriptors of individual lightning strikes, encompassing both Cloud-to-Ground (CG) and Intra-Cloud (IC) occurrences. Similar to the method in [72] that maps 1D data to 2D data processing, we map the temporospatial discretized lightning data to 3D. The map utilized to project the raw data maintains consistency with the reflectivity images covering the study area, featuring 480×480 grid points and a resolution of 0.01°×0.01°. Leveraging the recorded latitude and longitude of each strike, individual CG and IC strikes are aggregated into lightning density maps, representing 6-minute periods and serving as lightning observation images compatible with our network. Additionally, these lightning strikes contribute to the creation of labels. Given the strong coupling of CG and IC in the two-dimensional spatial projection, a pixel is assigned a value of 1 if a lightning event occurred at that location within the last hour; otherwise, it is set to 0.

2.3. Methodology

Due to the mesoscale/microscale characteristics (few minutes to hours in time, and tens to thousands of meters in space) of lightning phenomena in meteorology, the lightning density images/label images exhibit small scale, sparse (percentage of non-zero points on each lightning density image is only 0.5% on average), scattered (many non-zero pixels are not adjacent), and unclear boundary (lightning strikes are discontinuous in the image) features in the images. The U-Net architecture excels at extracting image features across multiple scales through a series of cascaded CNNs, utilizing skip connections to merge features and generate predictions at both coarse and fine levels, effectively addressing fine spatial details [73]. In light of these capabilities, a spatio-temporal fusion network is proposed based on the standard U-Net architecture in this paper. The proposed algorithm's encoder block integrates multi-branch and main path structures. Each branch and the main path are equipped with a spatial attention (SA) module to identify lightning-prone areas autonomously. Furthermore, a fusion module is introduced to amalgamate feature maps in the main path. The foundational framework is illustrated in Fig. 2.

2.3.1. Overall Architecture of Spatio-temporal Fusion Network for Lightning Nowcasting

U-Net is widely utilized for image segmentation tasks due to its excellent performance. Additionally, the 3D U-Net employs 3D CNN to extract features in the spatial-temporal dimension of the dataset [74]. Consider an image $X \in \mathbb{R}^{C\times H\times W\times D}$ with a spatial resolution of $H \times W$, C channels, and D depths (corresponding to the time dimension). The encoder block on the left in Fig. 2 encodes the inputs into high-level feature maps. The decoder block on the right decodes high-level feature maps back to the full spatial resolution, generating the corresponding pixel-wise label map. The output of the decoder is represented as an image $O_f \in \mathbb{R}^{N_c\times H\times W}$, where N_c is the number of label types.

In contrast to existing approaches, the proposed method's encoder block comprises both the main path and multiple branches, each corresponding to different data sources. These branches take inputs from different data sources to extract image features in convolutional layers. Subsequently, the feature maps outputted by the layers are fused in the main path. To extract coarse and fine features in the spatial-temporal domain of the input data sources, Spatial Attention (SA) modules and Fusion modules are introduced into the encoder block. The detailed explanations of these two components follow.

2.3.2. Spatial Attention

To automatically identify lightning areas, we employ the Spatial Attention (SA) mechanism. The detailed principle of SA is illustrated in Fig. 3. The SA module consists of a ReLU and a Sigmoid block. Each block incorporates a linear transformation channel-wise 1×1×1 convolution and a BatchNorm, followed by either ReLU or Sigmoid. The output O_l of the SA is:

$$O_l = \text{Sigmoid}(\text{Conv}(\text{ReLU}(\text{Conv}(X_l)))) \circ X_l \quad (1)$$

where, X_l is the input feature-map in layer l, $X_l \in \mathbb{R}^{F_l\times H_l\times W_l\times D_l}$, F is the number of channels, $\circ$ denotes

/

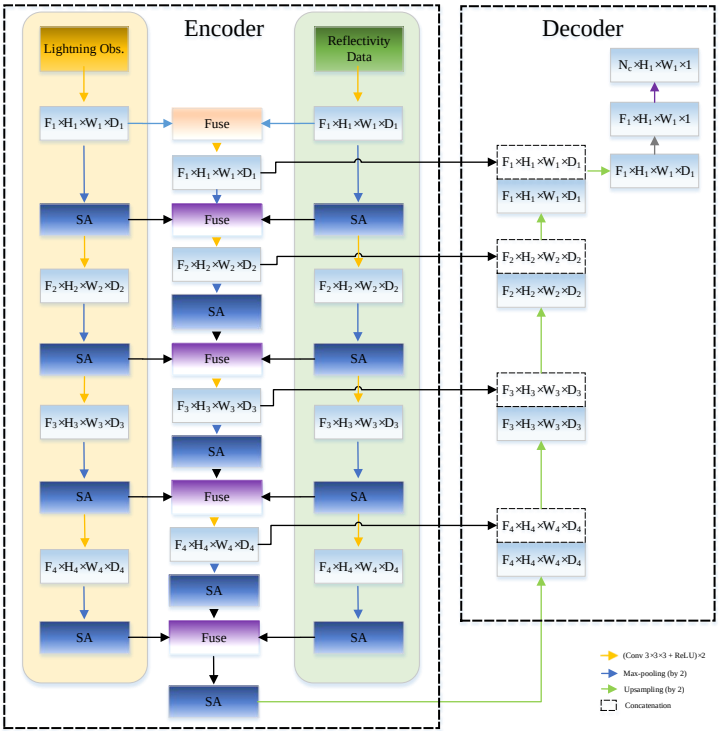

Fig. 2. The overall structure of Spatio-temporal Fusion Network (STF-LightNet). The STF-LightNet uses 3D U-Net architecture, which has the encoder-decoder block and the skip connections between the encoder and decoder. Within the encoder block, two branches are responsible for extracting features from distinct data sources, while the main path combines feature-maps from these branches along with those from the previous and current layers in the main path.

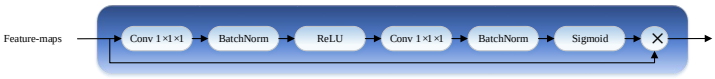

Fig. 3. Spatial attention module.

the Hadamard, the output is $O_l \in \mathbb{R}^{F_l \times H_l \times W_l \times D_l}$. The Spatial Attention (SA) module dynamically assigns probability weights to each grid of the input. High probabilities indicate focused regions, enhancing the features of the input feature-map, while low probabilities diminish their contributions.

2.3.3. Fusion Method

The fusion method shown as "Fuse" block in Fig. 2 enhances the exploitation of observation data features by combining the feature-maps output from the branches in the current layer and merging the feature-maps output from the previous- and current-layer in the main path. In this method, two types of fusion techniques are employed: the Weighted Fusion (WF) method and the Attention Gate Fusion (AGF) method. Detailed illustrations of WF and AGF are provided in Fig. 4 and Fig. 5 respectively. In both fusion methods, the process involves two steps: the first step combines the feature-maps from two branches, as depicted in the green dashed rectangle region in Fig. 4 and Fig. 5. The second step combines the fusion output of the current layer with the Spatial Attention (SA) output of the previous layer in the main path.

The Weighted Fusion (WF) method involves two steps of weighted fusion, while the Attention Gate Fusion (AGF) method comprises both a weighted fusion

/

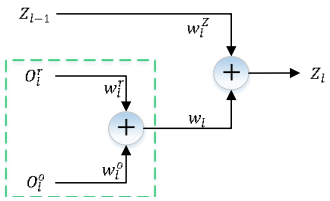

Fig. 4. Weighted fusion module.

(WF) and an Attention Gate (AG), with AG drawing inspiration from [75]. If O_l^r and O_l^o represent the feature-maps of radar reflectivity and lightning observations in layer l, the formulation for the first fusion step in both WF and AGF is as follows:

$$O_l^Z = w_l^r O_l^r + w_l^o O_l^o \tag{2}$$

where, O_l^Z is the output of first fusion step, $w_l^r, w_l^o \in \mathbb{R}$ are the scalar in layer l which are initialized to 1 and can be trained.

Then, let Z_{l-1} be the output of the previous layer in the main path, the second fusion step in WF is:

$$Z_l = w_l O_l^Z + w_l^Z Z_{l-1} \tag{3}$$

where weight $w_l, w_l^Z \in \mathbb{R}$ are the scalar in layer l which are initialized to 1 and can be trained. And, the second fusion step in AGF is:

$$\begin{aligned} Z_l = \text{Sigmoid}(\text{Conv}(\text{ReLU}(\text{Conv}(O_l^Z) \\ +\text{Conv}(Z_{l-1})))) \circ O_l^Z \end{aligned} \tag{4}$$

where, Z_l is the output of the Fusion method, and $\{O_l^r, O_l^o, Z_{l-1}, Z_l \in \mathbb{R}^{F_l \times H_l \times W_l \times D_l}\}$. The STF-LightNet using the Weighted Fusion (WF) module is named ST-WF-LightNet, while the STF-LightNet employing the Attention Gate (AG) fusion is named ST-AGF-LightNet.

2.3.4. Dataset

Lightning prediction involves nowcasting lightning events in the near future (e.g., within 0-2 hours) based on past and current observations. Given the strong spatial and temporal continuity of observations over a relatively short period, we leverage this property by constructing training samples with temporal information. Specifically, we utilize observations from the past half hour, including radar reflectivity and lightning observations, to nowcast lightning for the subsequent hour. With weather radar data produced at a 6-minute interval, there are 5 reflectivity maps within half an hour. Additionally, due to lightning density maps being accumulated every 6 minutes, there are 5 lightning maps within half an hour. These 5 maps for each data source in every half hour are stacked into a 4-dimensional training sample. The label corresponding to each sample is generated based on lightning observations in the hour following the end time of the sample. For a detailed explanation of how lightning density and labels are created, please refer to Section 2.2.2. The two sets of samples are separately fed to two branches at the encoder block. The shape of the sample is denoted as $X \in \mathbb{R}^{C \times H \times W \times D}$, where $C = 3$ and $D = 5$. The parameter $D = 5$ represents the number of maps in half an hour. Based on the structure of the dataset, the input/feature map sizes for each layer in the network encoder block are shown in Table 1, where F is the number of channels and $F = C$ for the input images at the beginning of the network.

Table 1. The layer size in each branch/main path of encoder block

Layer \ Size	$F \times H \times W \times D$
Input	$3 \times 480 \times 480 \times 5$
1	$64 \times 480 \times 480 \times 5$
2	$128 \times 240 \times 240 \times 4$
3	$256 \times 120 \times 120 \times 2$
4	$512 \times 60 \times 60 \times 1$
5	$1024 \times 30 \times 30 \times 1$

As our goal is to nowcast lightning, the effectiveness of the data for training the neural network increases with a higher occurrence of lightning within an hour. Consequently, we discarded samples with fewer than 30 lightning strikes in the corresponding labels. After this selection process, the dataset consists of 1641 samples of radar reflectivity and lightning observations. The dataset is divided into a training set and a test set. The test set encompasses 279 images, with the training set encompassing the remaining 1362 images. We used a validation set by randomly selecting 15% of the images belonging to the training set.

/

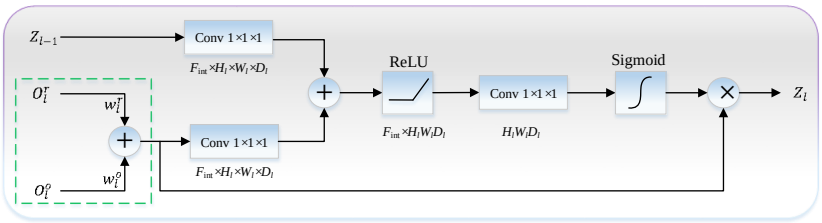

Fig. 5. Attention gate fusion module.

2.3.5. *Model Training, Validation, and Testing*

To prevent overfitting during the training process, it is essential to have a substantial number of samples. Dataset augmentation techniques, such as random mirroring and random rotations at 90°, were employed to enhance the diversity of the training samples. In Section 3, we presented the training results after data augmentation without directly comparing them to the results from unaugmented data. This comparison has already been extensively studied in the literature [61, 62, 71]. The cross-entropy loss, widely used for predicting the probability of a binary event, is expressed by the following formula:

$$\text{loss} = \frac{1}{N}\sum_{i=1}^{N}\sum_{c=0}^{1} y_c^i log[p_i^c] \tag{5}$$

where $c \in \{0,1\}$, N denotes the total pixel count, i represents an individual pixel, c_i indicates the label of pixel i, p_i denotes the probability associated with each pixel i, and c stands for the total number of classes.

Given the sparsity of lightning events in the observation maps, where the number of pixels without lightning events exceeds those with lightning events, the dataset exhibits an imbalance. To address this imbalance, we utilize in this study the weighted cross-entropy loss.

$$\text{loss}_w = \frac{1}{N}\sum_{i=1}^{N}\sum_{c=0}^{1} w_c^i y_c^i log[p_i^c] \tag{6}$$

where w_c is the weight coefficient associated with the class $c \in \{0,1\}$. We adopted the Inverse Frequency Weighted to give a higher weight to the less represented class:

$$w_c = (2f_c)^{-1} \tag{7}$$

where f_c is the frequency of that class, $f_0 + f_1 = 1$.

The optimizer function used is ADAM with a learning rate of 10^{-3}. ST-WF-LightNet has a total of 26,936,898 parameters, with 26,926,914 being trainable. On the other hand, ST-AGF-LightNet has a total of 28,350,678 parameters, with 28,333,006 being trainable. The batch size is set to 2. The training was conducted using a Tesla V100 GPU with 32GB of video memory and 32GB of RAM. With this hardware setup, one step required approximately 4 seconds for both STF-LightNets. An early stopping strategy was implemented: the learning rate is divided by 5 if the loss in the validation set does not improve for 3 epochs. In case there is no enhancement in the loss over six consecutive epochs, the training process is interrupted, and the model weights associated with the most optimal validation loss is preserved. The output of the network consists of a two-channel matrix, $O_f \in \mathbb{R}^{N_c \times H \times W}$, where $N_c = 2$. The nowcast probability for each grid point in the matrix is determined through the softmax classifier. Channel 0 corresponds to no lightning events, and channel 1 corresponds to lightning events.

2.3.6. *Evaluation*

When assessing the nowcasting performance of STF-LightNet, this study utilizes four traditional skill metrics: probability of detection (POD), false alarm ratio (FAR), threat score (TS), and equitable threat score (ETS). Let n be the total pixel count, while n_s, n_m, n_f, and n_c stand for the counts of TP (True Positive), FN (False Negative), FP (False Positive) and TN (True Negative), respectively. Detailed information on the four skill scores is provided in Table 2. To calculate the scores as mentioned above, deterministic nowcasts are required. Therefore, the probabilistic nowcasts, which are the network's output in chan-

/

nel 1, are transformed into deterministic ones using a given threshold T. In strict terms, TP is only considered when lightning falls within the predicted grid. However, as indicated in [76], neighborhood-based metrics demonstrate better characteristics when evaluating predictions on high-resolution grids compared to strict metrics. Therefore, this paper adopts the same neighborhood-based metric with a radius of 1, as used in [48], when evaluating nowcasting performance.

3. Results

Here, we present an identification performance comparison of the proposed ST-WF-LightNet and ST-AGF-LightNet with Light3DUnet [62] using the testing dataset. The lightning prediction network in [62] employed two baselines, U-Net and DeepLabV3+. Experimental results indicated that the lightning prediction network based on U-Net outperformed the one based on DeepLabV3+. Therefore, in this paper, our proposed algorithm is compared with Light3DUnet. However, the Light3DUnet used in this comparison incorporates the Attention Gate (AG) [75] in the decoder block, a departure from the original Light3DUnet [62]. Meanwhile, to observe the impact of the SA module on the network, the prediction results of the ST-AGF-LightNet without SA (called NoSA-AGF-LightNet) are given. We begin by examining the ability of these four networks to extract spatio-temporal features.

3.1. Network Model Analysis

Fig. 6 presents two cases of the prediction results for T+60 min on August 8, 2019, at two different times: T = 19:00 BJT and T = 19:30 BJT. Case 1 is illustrated in Figs. 6(a) - 6(g), while Case 2 is depicted in Figs. 6(h) - 6(n). Fig. 6(a)-Fig. 6(c) and Fig. 6(h)-Fig. 6(j) represent observations at 10-minute intervals over the past 30 minutes at T-20 $\sim$ T-30, T-10 $\sim$ T-20, and T-10 $\sim$ T. Fig. 6(d)-Fig. 6(g) and Fig. 6(k)-Fig. 6(n) display the contour plots of the lightning nowcasting for T+60 min generated by the four networks.

We first analyze the predicted outputs of STF-LightNets and Light3DUnet. Fig. 6(a)-Fig. 6(c) depict the movement and development of convective systems in the discussing region during the past 30 minutes for Case 1. Initially, there was one mesoscale convective system A, and two microscale convective systems B and C. Convective system A rapidly intensified and moved towards the southeast, accompanied by more and more lightning events, whereas convective system B gradually disappeared with fewer and fewer lightning events. Convective system C remained virtually unchanged for half an hour.

The prediction results shown in Fig. 6(d) - Fig. 6(g) correspond to the four networks for Case 1. Firstly, it is evident that all four networks can effectively capture the spatial and temporal features of the data. The networks anticipate the movement of lightning towards the southeast in the next hour and make accurate predictions for mesoscale lightning A. The distinction lies in the prediction output of STF-LightNets, considering both lightning observations and radar reflectivity, while Light3DUnet is more responsive to lightning observations. Consequently, STF-LightNet exhibits a broader prediction range and more accurate nowcasts for real convective systems and lightning locations, while Light3DUet excels in accurately nowcasting dense lightning areas. This suggests that although all the above models are based on 3DUnet architecture and also use AG modules. However, the network proposed in this paper adopts a multi-branch + main path for feature extraction and fusion, where the branch part effectively extracts the features of different data sources and fuses them in the main path, which makes the network learn the spatio-temporal characteristics of different data sources at the same time. While Light3DUnet did lose some of the features of the radar reflectivity images during the feature extraction process. Obviously, the use of multi-branches + main path for feature extraction and fusion in the encoder stage is superior to the use of the AG module for feature fusion in the decoder stage.

Secondly, we observe that STF-LightNets possess the ability to nowcast microscale lightning, represented as dots in A, B, and C in Figs. 6(d), 6(e) and 6(f). However, Light3DNet lacks this capability and misses microscale lightning B and C. This further confirms that the strategy of using multi-branch + main path effectively extracts and restores features from different data sources.

Similar conclusions can be drawn from Fig. 6(k)-Fig. 6(n) for Case 2, where Fig. 6(k) - Fig. 6(m) repre-

/

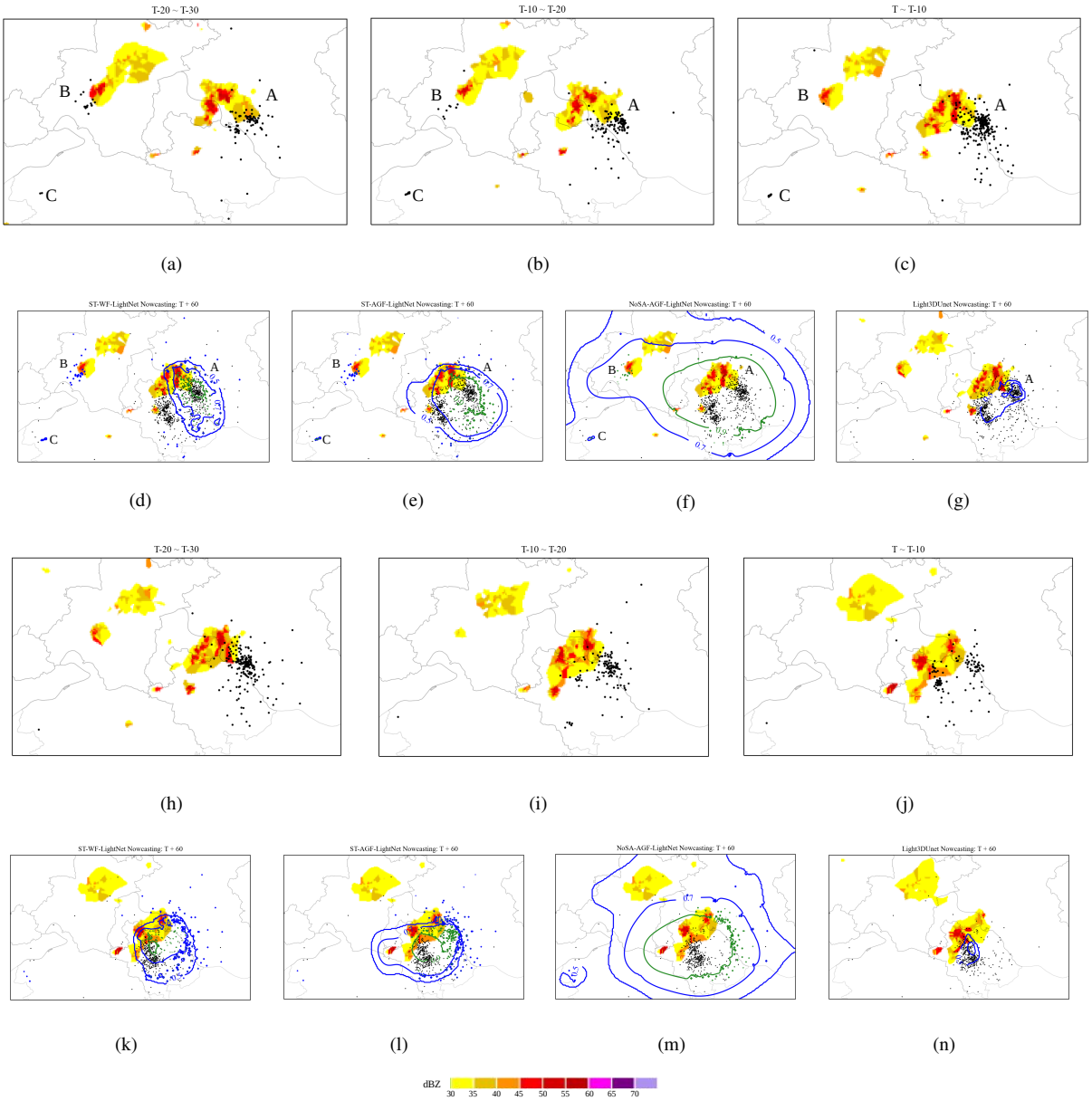

Fig. 6. Two cases of lightning nowcasting for the next 0-60 min of three networks and the observations of the past 30 min, case one is (a)-(g), case two is (h)-(n). The (a)-(c) and (h)-(j) are the observations for the past 30 min at 10 min intervals. The (d)-(g) and (k)-(n) are the contour plots of lightning nowcasting, which show the nowcast probabilities of 0.5, 0.7, and 0.9 in the colors blue, blue, and green respectively. The black dots denote lightning observations, while the color-shaded areas are radar reflectivity which is retained only if the intensity is greater than or equal to 30 dBZ. The (a) (h) are the past observations from T-20 to T -30. The (b) (i) are the past observations from T-10 to T -20. The (c) (j) are the past observations from T to T -10. The (d) (k) are ST-WF-LightNet Nowcasting for T+60 with the ground-truth. The (e) (l) are ST-AGF-LightNet Nowcasting for T+60 with the ground-truth. The (f) (m) are NoST-AGF-LightNet Nowcasting for T+60 with the ground-truth. The (g) (n) are Light3DUnet Nowcasting for T+60 with the ground-truth.

/

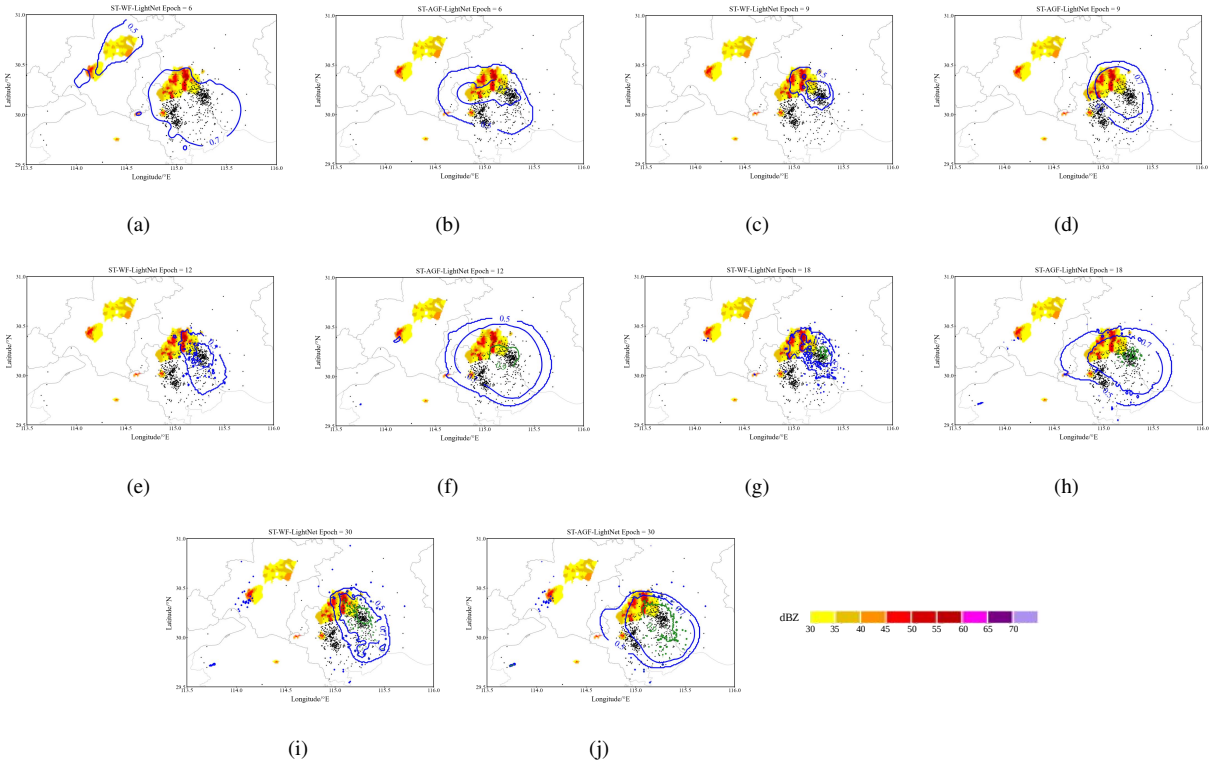

Fig. 7. Lightning nowcasting by ST-WF-LightNet and ST-AGF-LightNet for next 0-60 min across different training epochs (6, 9, 12, 18, 30). The left column is the contour plots of ST-WF-LightNet lightning nowcasting, and the right column is the contour of ST-AGF-LightNet. The nowcast probabilities of 0.5, 0.7, and 0.9 are shown in the colors blue, blue, and green respectively. The black dots denote lightning observations, while the color-shaded areas are radar reflectivity which is retained only if the intensity is greater than or equal to 30 dBZ.

sent STF-LightNets' predictions, and Fig. 6(n) represents Light3DUnet's prediction.

Next, we delve into the discussion of two STF-LightNets utilizing different fusion strategies. Let's begin by examining Case 1. By comparing Fig. 6(d) and Fig. 6(e), it is evident that ST-WF-LightNet captures less information in the time dimension compared to ST-AGF-LightNet. Consequently, for convective system A, which exhibits temporal movement, ST-WF-LightNet provides predictions at the same location solely based on the past half-hour of observations, resulting in a loss of predictions for newly developed lightning. In contrast, ST-AGF-LightNet acquires more temporal information for inferring the motion of the convective system, leading to more reasonable nowcasts.

Turning to Case 2, a similar trend is observed in Fig. 6(k) and Fig. 6(l). The contour regions provided by ST-AGF-LightNet, with probabilities of 0.5, 0.7, and 0.9, respectively, are all larger than those produced by ST-WF-LightNet.

Finally, comparing SA-AGF-LightNet with NoSA-AGF-LightNet, as shown in Fig. 6(e), Fig. 6(l) and Fig. 6(f), Fig. 6(m), we found that due to the absence of the SA module, the feature maps extracted by the branches lack finer details. During main path fusion, there is a tendency to directly merge the two features. Therefore, as seen in Fig. 6(f), the contour lines with high probabilities directly encompass both lightning areas and radar reflectivity areas, without effectively integrating the detailed features of both.

3.2. Visualization Analysis of Network

Here, we present a visualization of the results obtained from STF-LightNets to analyze the network's

/

functioning. The lightning nowcasting pertains to the period from 19:00 to 20:00 BJT on 8 August 2019. In Fig. 7, the lightning nowcasting results are depicted concerning training epochs (6, 9, 12, 18, 30) for both ST-WF-LightNet and ST-AGF-LightNet.

A common observation reveals that both proposed networks undergo gradual updates, with a focus on localizing the lightning areas and the boundaries of convection systems. Moreover, both algorithms initially provide a broad outline of the convection system at coarser scales during the early stages of training. As training progresses, more detailed information and irregular boundary details are extracted. Subsequently, not only is a fine outline of the mesoscale lightning area gradually predicted, but point predictions for scattered, microscale lightning, and the boundaries of convection systems are also provided at finer resolutions. This is evident as the blue and green dots gradually appear with increasing training epochs, as illustrated in Fig. 7(g) - Fig. 7(j).

3.3. Nowcast Performance

This section assesses the performance of lightning nowcasting for ST-WF-LightNet, ST-AGF-LightNet and Light3DUnet. Initially, two widely utilized metrics for evaluating image classification algorithm performance are introduced: the receiver operating characteristic (ROC) and the area under the curve (AUC), presented in Fig. 8. It can be observed that, compared to Light3DUnet, the ROC curve of STF-LightNet is closer to the upper-left corner, and the AUC is closer to 1. This indicates that the performance of the STF-LightNet model is superior to Light3DUnet. Furthermore, among the two STF-LightNet methods, ST-AGF-LightNet outperforms ST-WF-LightNet.

Using the ROC curves, we calculated the Youden index to determine the optimal thresholds, which are $T_W = 0.7$ for ST-WF-LightNet, $T_{AG} = 0.8$ for ST-AGF-LightNet and $T_U = 0.5$ for Light3DUnet based on the maximum Youden index, respectively.

Utilizing the optimal thresholds $T_W = 0.7$, $T_{AG} = 0.8$ and $T_U = 0.5$, we compute the four metrics mentioned in Section 2.3.6 to assess the performance of the three algorithms. The results are presented in Table 2. By definition of the skill scores, for POD, TS, and ETS, larger is better, and for FAR, smaller is better. In table 2, we have underlined the best scores for three methods. Remarkably, both STA-LightNet methods demonstrate superior performance compared to the Light3DUnet method in terms of POD scores, TS scores, and ETS scores, despite some minor shortcomings in FAR. It is important to acknowledge that an improvement in POD might result in a proportional increase in FAR. However, the STF-LightNet models notably enhance POD, TS, and ETS with only a marginal increase in FAR. Additionally, the performance of ST-AGF-LightNet is superior to that of ST-WF-LightNet. Consequently, the ST-AGF-LightNet model exhibits advantages such as a high detection rate, robust resolution capability, and stability.

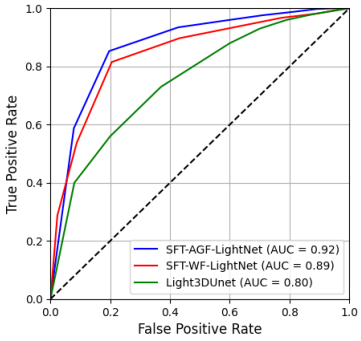

Fig. 8. ROC and AUC of one-hour lightning nowcasting produced by ST-WF-LightNet, ST-AGF-LightNet and Light3DUnet for the testing dataset. False positive rate = $n_f/(n_f+n_c)$ and true positive rate = $n_s/(n_s+n_m)$.

Table 2. Skill scores of lightning 0-1 hour nowcasting results by STF-LightNet and Light3DUnet on testing set. The equations of POD, FAR, TS and ETS are presented in the table, where n, n_s, n_m, n_f and n_c are defined in Section 2.3.6, and $r = (n_s+n_f)\times(n_s+n_m)/n$ is the expectation of the number of lightning hits in random nowcasts.

Method	POD $\frac{n_s}{(n_s+n_m)}$	FAR $\frac{n_f}{(n_s+n_f)}$	TS $\frac{n_s}{(n_s+n_m+n_f)}$	ETS $\frac{(n_s-r)}{(n_s+n_m+n_f-r)}$
SA-WF-LightNet	0.815	0.589	0.398	0.386
SA-AGF-LightNe	<u>0.854</u>	0.570	<u>0.422</u>	<u>0.405</u>
Light3DUnet	0.731	<u>0.512</u>	0.382	0.373

The differences in optimal thresholds for the two STF-LightNets indicate variations in the distribution of probability matrices output by the two networks. For a more in-depth analysis, we statistically averaged all the probability nowcast outputs greater than 0.5 obtained on the testing dataset and created a his-

/

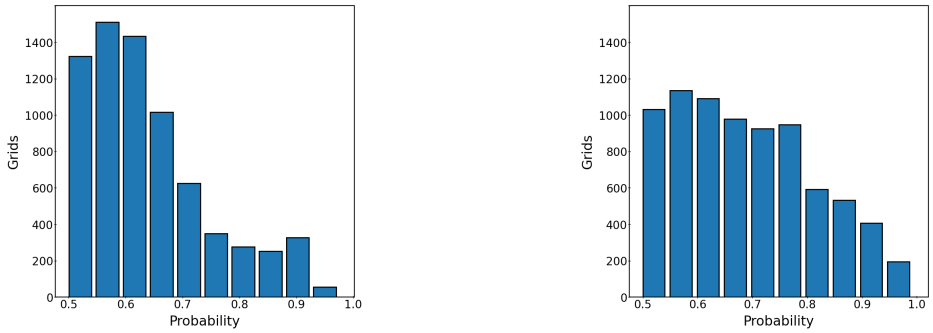

Fig. 9. The histogram for all prediction results obtained on the validation dataset for two STF-LightNets: (a) ST-WF-LightNet; (b) ST-AGF–LightNet.

togram, as shown in Fig. 9. First, let's explain why we only count grids with probability values greater than 0.5. As known in section 2.3.5, the network outputs a probability matrix with two channels, where the sum of probability values for grids in channels 0 and 1 equals 1. Channel 1 corresponds to the probability of lightning occurrence. Before determining the optimal threshold, we assume that grids with probability values greater than 0.5 indicate lightning occurrence. Therefore, we only tally grids with probability values exceeding 0.5 at this stage. From Fig. 9, it can be observed that the probability values of ST-WF-LightNet are mainly distributed between 0.5 and 0.7, while the probability values of ST-AGF-LightNet are distributed between 0.6 and 0.8. To quantify this, we calculated the percentage of grids with probability values greater than 0.7: 24.3% for ST-WF-LightNet and 45.6% for ST-AGF-LightNet. This indicates that the grids in ST-AGF-LightNetd attain higher probability values, and these elevated values are achieved by the automatic recognition of lightning regions and the assignment of high weights by the attention gate fusion module.

3.4. Visualization Results

Fig. 10 visualizes typical lightning nowcasting for the next hour using the two proposed algorithms. Fig. 10(a) and Fig. 10(b) present the results for ST-WF-LightNet and ST-AGF-LightNet every half hour from 14:30 to 17:30, respectively. Each subfigure, from left to right, corresponds to the time at 14:30, 15:00, 15:30, 16:00, 16:30, 17:00, and 17:30 BJT on 2 August 2019, respectively. The red dots represent TP, blue dots denote FN, and green dots indicate FP, using the optimal threshold obtained in Section 3.3. As observed in Fig. 10, the lightning nowcasting of both algorithms appears promising. The algorithms provide more precise details for the boundaries of mesoscale convective systems, and for microscale convective systems, they offer scattered point-like nowcasting. Furthermore, the visualization results in Fig. 10 align with the skill scores in Table 2, confirming that the nowcasting performance of ST-AGF-LightNet surpasses that of ST-WF-LightNet.

4. Conclusion and future works

In this paper, we introduce a spatio-temporal fusion deep learning lightning nowcasting network (STF-LightNet), which comprises ST-WF-LightNet based on weighted summation fusion and ST-AGF-LightNet based on attention gate fusion. These variations arise from different fusion methods employed in the main path within the encoder block. The network is assessed using observational data from central China, encompassing radar reflectivity images and lightning observation data. Experimental results demonstrate the robust capabilities of STF-LightNets for lightning nowcasting. The predictions not only delineate the boundaries of mesoscale convective regions but also nowcast microscale convective regions in the form of scattered spots. This success is attributed to the multi-branches + main path structure, incorporating spatial attention and fusion modules. Firstly, the multi-branches + main path structure allows the network to extract and con-

/

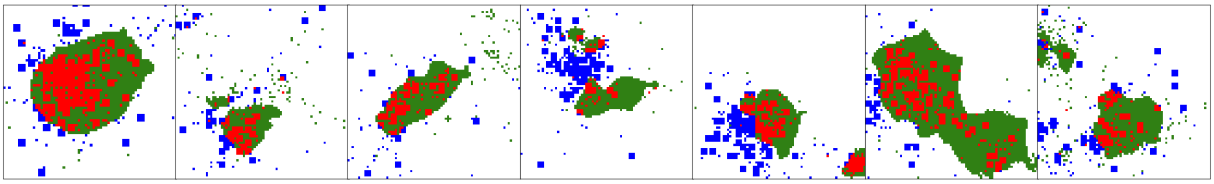

(a)

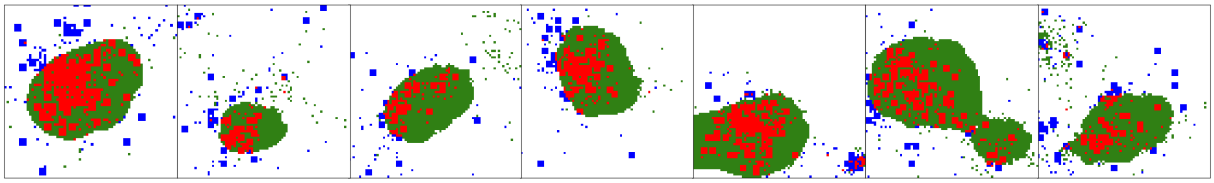

(b)

Fig. 10. The one-hour lightning nowcasting results of two STF-LightNets: (a) ST-WF-LightNet; (b) ST-AGF-LightNet. For each subfigure, from left to right, there are 7 moments of 2 August 2019 at 14:30, 15:00, 15:30, 16:00, 16:30, 17:00 and 17:30 BJT, respectively. The red dots denote TP, blue dots denote FN, and green dots denote FP.

solidate features from diverse data sources, evident in the nowcasting outputs displaying the edge profile of radar reflectivity images while focusing on lightning areas. Secondly, the spatial attention module and fusion module automatically identify and enhance lightning regions, enabling predictions that reveal the fine irregular boundaries of mesoscale convective regions and the scattered spots of microscale convective areas. The use of the inverted frequency-weighted cross-entropy loss function further enhances less common classes in the images, thereby improving the probabilistic output of the network. Finally, in terms of fusion methods, the attention gate fusion method outperforms the weighted summation fusion method. Compared to ST-WF-LightNet, ST-AGF-LightNet acquires more timely information, resulting in superior performance. ROC curve analysis and Youden index calculations aid in determining optimal thresholds for the two STF-LightNets.

The incorporation of the multi-branches + main path structure for processing multi-source data and fusing features is pivotal for achieving optimal nowcasting performance in this study. Additional work can be pursued in three main areas. Firstly, expanding data sources involves integrating satellite data, automatic weather station (AWS) data, and digital elevation model (DEM) data, with a preference for high-resolution AWS observational data. Secondly, implementing a multi-task model is essential for simultaneously predicting precipitation and lightning. While this paper predominantly focuses on lightning nowcasting, which involves a binary classification task for each grid in the image, a multi-task model could extend the capabilities of the algorithm. Thirdly, explore newer and sophisticated supervised machine learning/classification algorithms [77–79] to enhance nowcasting performance.

5. Acknowledgments

This work is supported by the High-Level Talent Project of Chengdu Normal University (No. YJRC2020-12), China Scholarship (No. 202208515065), Key Laboratory of Featured Plant Development and Research in Sichuan Province (No. TSZW2110), Jiangsu Distinguished Professor programme, and the National Natural Science Foundation of China(No. 62341202).

References

[1] J. Wang, S. Gao, L. Yu, X. Liu, F. Neri, D. Zhang, and L. Kou, “Uncertainty-aware trustworthy weather-driven failure risk predictor for overhead contact lines,” *Reliability*

Engineering & System Safety, vol. 242, p. 109734, 2024. [Online]. Available: https://www.sciencedirect.com/science/article/pii/S0951832023006488

[2] P. N. Gatlin and S. J. Goodman, "A total lightning trending algorithm to identify severe thunderstorms," *J. Atmos. Oceanic Technol.*, vol. 27, pp. 3–7, 2010.

[3] D. J. C. Stensrud, "Progress and challenges with warn-on-forecast," *Atmos. Res.*, vol. 123, pp. 2–16, 2013.

[4] B. H. Lynn, C. Yair, G. Price, A. J. Kelman, and A. J. Clark, "Predicting cloud-to-ground and intracloud lightning in weather forecast models," *Wea. Forecasting*, vol. 27, p. 1470–1488, 2012.

[5] C. Farnell, T. Rigo, and N. Pineda, "Lightning jump as a nowcast predictor: Application to severe weather events in catalonia," *Atmos. Res.*, vol. 183, p. 130–141, 2017.

[6] C. J. Schultz, L. D. Carey, E. V. Schultz, and R. J. Blakeslee, "Kinematic and microphysical significance of lightning jumps versus nonjump increases in total flash rate," *Wea. Forecasting*, vol. 32, p. 275–288, 2017.

[7] W. C. Woo and W. K. Wong, "Operational application of optical flow techniques to radar-based rainfall nowcasting," *Atmosphere*, vol. 8, p. 48, 2017.

[8] R. Bechini and V. Chandrasekar, "An enhanced optical flow technique for radar nowcasting of precipitation and winds," *J. Atmos. Oceanic Technol.*, vol. 34, p. 2637–2658, 2017.

[9] C. J. Schultz, L. D. Carey, E. V. Schultz, and R. J. Blakeslee, "Development of a precipitation nowcasting algorithm based upon optical flow techniques," *Journal of Hydrology*, vol. 288, no. 1-2, p. 74–91, 2004.

[10] C. J. Schultz, L. D. Carey, E. V. Schultz, and R. J. Blakeslee, "A probabilistic precipitation forecasting scheme which merges an extrapolation nowcast with downscaled nwp," *Quarterly Journal of the Royal Meteorological Society*, vol. 132, no. 620, p. 2127–2155, 2006.

[11] M. Dixon and G. Wiener, "Titan: Thunderstorm identification, tracking, analysis, and nowcasting—a radar-based methodology," *J. Atmos. Ocean. Technol.*, vol. 10, p. 785–797, 1993.

[12] J. Johnson, P. MacKeen, A. Witt, E. Mitchell, G. Stumpf, M. Eilts, and K. Thomas, "The storm cell identification and tracking algorithm: An enhanced wsr-88d algorithm," *Wea. Forecasting*, vol. 13, p. 263–276, 1998.

[13] L. Han, J. Sun, W. Zhang, Y. Xiu, H. Feng, and Y. Lin., "A machine learning nowcasting method based on real-time reanalysis data," *J. Geophys. Res. Atmos.*, vol. 122, p. 4038–4051, 2017.

[14] J. Leinonen, U. Hamann, U. Germann, and J. Mecikalski, "Nowcasting thunderstorm hazards using machine learning: The impact of data sources on performance," *Nat. Hazards Earth Syst. Sci.*, vol. 22, p. 577–597, 2021.

[15] Buendia-Buendia, F. S., G. Buendia, and D. Andina, "Determining geostrophic wind direction in a rainfall forecast expert system," *Integrated Computer-Aided Engineering*, no. 1, p. 111 – 121, 2019.

[16] Y. Xue, H. Zhu, and F. Neri, "A self-adaptive multi-objective feature selection approach for classification problems," *Integrated Computer-Aided Engineering*, vol. 29, pp. 3–21, 2022.

[17] A. La Fata, F. Amato, M. Bernardi, M. D'Andrea, R. Procopio, and E. Fiori, "Cloud-to-ground lightning nowcasting using machine learning," in *2021 35th International Conference on Lightning Protection (ICLP) and XVI International Symposium on Lightning Protection (SIPDA)*, vol. 1. IEEE, 2021, pp. 1–6.

[18] J. R. Mecikalski, X. Li, L. D. Carey, E. W. McCaul, and T. A. Coleman, "Regional comparison of goes cloud-top properties and radar characteristics in advance of first-flash lightning initiation," *Mon. Wea. Rev.*, vol. 141, p. 55–74, 2013.

[19] L. Foresti, M. Reyniers, A. Seed, and L. Delobbe, "Development and verification of a real-time stochastic precipitation nowcasting system for urban hydrology in belgium," *Hydrology and Earth System Sciences*, vol. 20, no. 1, p. 505–527, 2016.

[20] J. Sun, H. Li, and H. Adeli, "Concept drift-oriented adaptive and dynamic support vector machine ensemble with time window in corporate financial risk prediction," *IEEE Trans. Syst. Man Cybern. Syst.*, vol. 43, no. 4, pp. 801–813, 2013. [Online]. Available: https://doi.org/10.1109/TSMCA.2012.2224338

[21] J. P. Amezquita-Sanchez, M. Valtierra-Rodriguez, H. Adeli, and C. A. Perez-Ramirez, "A novel wavelet transform-homogeneity model for sudden cardiac death prediction using ECG signals," *J. Medical Syst.*, vol. 42, no. 10, pp. 176:1–176:15, 2018. [Online]. Available: https://doi.org/10.1007/s10916-018-1031-5

[22] G. Mirzaei and H. Adeli, "Machine learning techniques for diagnosis of alzheimer disease, mild cognitive disorder, and other types of dementia," *Biomed. Signal Process. Control.*, vol. 72, no. Part, p. 103293, 2022. [Online]. Available: https://doi.org/10.1016/j.bspc.2021.103293

[23] H. Adeli, S. Ghosh-Dastidar, and N. Dadmehr, "A spatio-temporal wavelet-chaos methodology for eeg-based diagnosis of alzheimer's disease," *Neuroscience letters*, vol. 444, no. 2, pp. 190–194, 2008.

[24] M. Ahmadlou, H. Adeli, and A. Adeli, "Spatiotemporal analysis of relative convergence of eegs reveals differences between brain dynamics of depressive women and men," *Clinical EEG and neuroscience*, vol. 44, no. 3, pp. 175–181, 2013.

[25] W. Qiu, W. ShangGuan, B. Cai, and L. Chai, "Heterogeneous data-based spatiotemporal trajectory synchronization for virtual–real interactive testing," *Computer-Aided Civil and Infrastructure Engineering*, vol. 38, no. 1, pp. 49–66, 2023.

[26] Y. Dong, S. Patil, B. van Arem, and H. Farah, "A hybrid spatial–temporal deep learning architecture for lane detection," *Computer-Aided Civil and Infrastructure Engineering*, vol. 38, no. 1, pp. 67–86, 2023.

[27] P. Xie, S. Hao, J. Zhao, Z. Liang, and X. Li, "A spatio-temporal method for extracting gamma-band features to enhance classification in a rapid serial visual presentation task," *International Journal of Neural Systems*, vol. 32, no. 3, p. 2250010, 01 2022.

[28] K. Raeisi, M. Khazaei, G. Tamburro, P. Croce, S. Comani, F. Zappasodi *et al.*, "A class-imbalance aware and explainable

spatio-temporal graph attention network for neonatal seizure detection," *International Journal of Neural Systems*, vol. 33, no. 9, p. 2350046, 2023.

[29] A. Hassanpour, M. Moradikia, H. Adeli, S. R. Khayami, and P. Shamsinejadbabaki, "A novel end-to-end deep learning scheme for classifying multi-class motor imagery electroencephalography signals," *Expert Syst. J. Knowl. Eng.*, vol. 36, no. 6, 2019. [Online]. Available: https://doi.org/10.1111/exsy.12494

[30] G. B. Martins, J. P. Papa, and H. Adeli, "Deep learning techniques for recommender systems based on collaborative filtering," *Expert Syst. J. Knowl. Eng.*, vol. 37, no. 6, 2020. [Online]. Available: https://doi.org/10.1111/exsy.12647

[31] H. S. Nogay and H. Adeli, "Diagnostic of autism spectrum disorder based on structural brain MRI images using, grid search optimization, and convolutional neural networks," *Biomed. Signal Process. Control.*, vol. 79, no. Part, p. 104234, 2023. [Online]. Available: https://doi.org/10.1016/j.bspc.2022.104234

[32] H. S. Nogay and H. Adeli, "Machine learning (ml) for the diagnosis of autism spectrum disorder (asd) using brain imaging," *Reviews in the Neurosciences*, vol. 31, no. 8, pp. 825–841, 2020. [Online]. Available: https://doi.org/10.1515/revneuro-2020-0043

[33] H. S. Nogay and H. Adeli, "Detection of epileptic seizure using pretrained deep convolutional neural network and transfer learning," *European Neurology*, vol. 83, pp. 602–614, 01 2020.

[34] M. H. Rafiei, L. V. Gauthier, H. Adeli, and D. Takabi, "Self-supervised learning for electroencephalography," *IEEE Transactions on Neural Networks and Learning Systems*, 2022.

[35] H. S. Nogay and H. Adeli, "Multiple classification of brain mri autism spectrum disorder by age and gender using deep learning," *Journal of Medical Systems*, vol. 48, 2024.

[36] P. j. Chun, T. Yamane, and Y. Maemura, "A deep learning-based image captioning method to automatically generate comprehensive explanations of bridge damage," *Computer-Aided Civil and Infrastructure Engineering*, vol. 37, 11 2021.

[37] A. Olamat, P. Kiziloglu, and S. Atasever, "Deep learning methods for multi-channel eeg-based emotion recognition," *International Journal of Neural Systems*, vol. 32, 04 2022.

[38] K. Bi, L. Xie, H. Zhang, X. Chen, X. Gu, and Q. Tian, "Pangu-weather: A 3d high-resolution model for fast and accurate global weather forecast," *arXiv 2022, arXiv:2211.02556.*, 2022.

[39] L. Chen, X. Zhong, F. Zhang, Y. Cheng, Y. Xu, Y. Qi, and H. Li, "Fuxi: A cascade machine learning forecasting system for 15-day global weather forecast," *arXiv 2023, arXiv: 2306.12873*, 2023.

[40] K. Chen, T. Han, J. Gong, and et al., "Fengwu: Pushing the skillful global medium-range weather forecast beyond 10 days lead," *arXiv 2023, arXiv: 2304.02948*, 2023.

[41] R. Lam, A. Sanchez-Gonzalez, M. Willson, and et al., "Graphcast: Learning skillful medium-range global weather forecasting," *arXiv 2023, arXiv:2212.12794v2*, 2023.

[42] J. P., S. S., P. H., and et al., "Fourcastnet: A global data-driven high-resolution weather model using adaptive fourier neural operators," *arXiv 2022, arXiv:2202.11214*, 2022.

[43] M. S. Shahabi, A. Shalbaf, B. Nobakhsh, R. Rostami, and R. Kazemi, "Attention-based convolutional recurrent deep neural networks for the prediction of response to repetitive transcranial magnetic stimulation for major depressive disorder," *Int. J. Neural Syst.*, vol. 33, no. 2, pp. 2 350 007:1–2 350 007:13, 2023. [Online]. Available: https://doi.org/10.1142/S0129065723500077

[44] B. K. Oh, S. H. Yoo, and H. S. Park, "A measured data correlation-based strain estimation technique for building structures using convolutional neural network," *Integr. Comput. Aided Eng.*, vol. 30, no. 4, pp. 395–412, 2023. [Online]. Available: https://doi.org/10.3233/ICA-230714

[45] D. S. Jodas, T. Yojo, S. Brazolin, G. D. N. Velasco, and J. P. Papa, "Detection of trees on street-view images using a convolutional neural network," *Int. J. Neural Syst.*, vol. 32, no. 1, pp. 2 150 042:1–2 150 042:20, 2022. [Online]. Available: https://doi.org/10.1142/S0129065721500428

[46] X. Shi, Z. Chen, H. Wang, D. Yeung, W. Wong, and W. Woo, "Convolutional lstm network: A machine learning approach for precipitation nowcasting," in *In Proceedings of the 29th Conference on Neural Information Processing Systems(NeurIPS)*, 2015.

[47] X. Shi, Z. Gao, L. Lausen, Wang, Y. H., D.Y., and W. Wong, "Deep learning for precipitation nowcasting: A benchmark and a new model," in *In Proceedings of the 31st Conference on Neural Information Processing Systems(NeurIPS)*, 2017.

[48] Y.-A. Geng, Q. Li, T. Lin, L. Jiang, L. Xu, Z. Dong, W. Yao, W. Lyu, and Y. Zhang, "Lightnet: A dual spatiotemporal encoder network model for lightning prediction," in *In Proceedings of the 25th ACM SIGKDD International Conference on Knowledge Discovery & Data Mining*, 2019.

[49] Y.-A. Geng, Q. Li, T. Lin, W. Yao, L. Xu, Z. Dong, D. Zheng, and X.-Y. Zhou, "A deep learning framework for lightning forecasting with multi-source spatiotemporal data," *Q. J. R. Meteorol. Soc.*, vol. 147, p. 4048–4062, 2021.

[50] J. Leinonen, U. Hamann, and U. Germann, "Seamless lightning nowcasting with recurrent-convolutional deep learning," *arXiv:2203.10114v1 [physics.ao-ph] 15 Mar 2022*, 2022.

[51] J. Leinonen, U. Hamann, I. V. Sideris, and U. Germann, "Thunderstorm nowcasting with deep learning: A multi-hazard data fusion model," *Geophysical Research Letters*, vol. 50, p. e2022GL101626, 2023.

[52] M. Lu, C. Jin, M. Yu, Q. Zhang, H. Liu, Z. Huang, and T. Dong, "Mcgln: A multimodal convlstm-gan framework for lightning nowcasting utilizing multi-source spatiotemporal data," *Atmospheric Research*, vol. 297, p. 107093, 2024. [Online]. Available: https://www.sciencedirect.com/science/article/pii/S0169809523004908

[53] I. Goodfellow, J. Pouget-Abadie, M. Mirza, B. Xu, D. Warde-Farley, S. Ozair, A. Courville, and Y. Bengio, "Generative adversarial networks," *Commun. ACM*, vol. 63, no. 11, p. 139–144, oct 2020. [Online]. Available: https://doi.org/10.1145/3422622

[54] H. Wu, F. He, Y. Duan, and X. Yan, "Perceptual metric-

guided human image generation," *Integrated Computer-Aided Engineering*, vol. 29, no. 2, pp. 141–151, 3 2022.

[55] M. Sadeghi, P. Nguyen, K. Hsu, and S. Sorooshian, "Improving near real-time precipitation estimation using a u-net convolutional neural network and geographical information," *Environ. Model. Softw.*, vol. 134, p. 104856, 2020.

[56] I. G. Aguilar, J. García-González, R. M. Luque-Baena, E. López-Rubio, and E. Domínguez, "Optimized instance segmentation by super-resolution and maximal clique generation," *Integrated Computer-Aided Engineering*, vol. 30, pp. 243–256, 2023.

[57] N. Mammone, C. Ieracitano, H. Adeli, and F. Morabito, "Autoencoder filter bank common spatial patterns to decode motor imagery from eeg," *IEEE Journal of Biomedical and Health Informatics*, vol. 27, no. 5, pp. 2365–2376, 2023.

[58] J. Chen and Y. He, "A novel u-shaped encoder–decoder network with attention mechanism for detection and evaluation of road cracks at pixel level," *Computer-Aided Civil and Infrastructure Engineering*, vol. 37, no. 13, pp. 1721–1736, 2 2022.

[59] F. Celik and M. König, "A sigmoid-optimized encoder–decoder network for crack segmentation with copy-edit-paste transfer learning," *Computer-Aided Civil and Infrastructure Engineering*, vol. 37, no. 14, pp. 1875–1890, 04 2022.

[60] V. Giglioni, I. Venanzi, V. Poggioni, A. Milani, and F. Ubertini, "Autoencoders for unsupervised real-time bridge health assessment," *Computer-Aided Civil and Infrastructure Engineering*, vol. 38, no. 8, pp. 959–974, 11 2022.

[61] K. Zhou, Y. Zheng, W. Dong, and T. Wang, "A deep learning network for cloud-to-ground lightning nowcasting with multisource data," *J. Appl. Meteor. Climatol.*, vol. 37, p. 927–942, 2020.

[62] L. Fan and C. Zhou, "Cloud-to-ground and intra-cloud nowcasting lightning using a semantic segmentation deep learning network," *Remote Sens.*, vol. 15, p. 4981, 2023.

[63] P. Sharma, Y. U. Khan, O. Farooq, M. Tripathi, and H. Adeli, "A wavelet-statistical features approach for nonconvulsive seizure detection," *Clinical EEG and neuroscience*, vol. 45, no. 4, pp. 274–284, 2014.

[64] U. R. Acharya, V. K. Sudarshan, H. Adeli, J. Santhosh, J. E. Koh, S. D. Puthankatti, and A. Adeli, "A novel depression diagnosis index using nonlinear features in eeg signals," *European neurology*, vol. 74, no. 1-2, pp. 79–83, 2015.

[65] H. Qarib and H. Adeli, "A new adaptive algorithm for automated feature extraction in exponentially damped signals for health monitoring of smart structures," *Smart Materials and Structures*, vol. 24, no. 12, p. 125040, 2015.

[66] W. Ye, J. Ren, A. A. Zhang, and C. Lu, "Automatic pixel-level crack detection with multi-scale feature fusion for slab tracks," *Computer-Aided Civil and Infrastructure Engineering*, vol. 38, no. 18, pp. 2648–2665, 2023.

[67] D.-C. Feng, Y.-P. Liang, X. Ren, and J. Li, "Random fields representation over manifolds via isometric feature mapping-based dimension reduction," *Computer-Aided Civil and Infrastructure Engineering*, vol. 37, no. 5, pp. 593–611, 2022.

[68] Y. Tian, C. Ding, Y. F. Lin, S. Ma, and L. Li, "Automatic feature type selection in digital photogrammetry of piping," *Computer-Aided Civil and Infrastructure Engineering*, vol. 37, no. 10, pp. 1335–1348, 2022.

[69] Z. Yu, L. Albera, R. Le Bouquin Jeannes, A. Kachenoura, A. Karfoul, C. Yang, and H. Shu, "Epileptic seizure prediction using deep neural networks via transfer learning and multi-feature fusion," *International Journal of Neural Systems*, vol. 32, no. 07, p. 2250032, 2022.

[70] Y. Zhu, Y. Wang, H. Chen, Z. Guo, and Q. Huang, "Large-scale image retrieval with deep attentive global features," *International Journal of Neural Systems*, vol. 33, no. 03, p. 2350013, 2023.

[71] Q. 31. Huang, S. Chen, and J. Tan, "Tsrc: A deep learning model for precipitation short-term forecasting over china using radar echo data," *Remote Sens.*, vol. 15, p. 142, 2023.

[72] A. Morrone, W. Anderson, and S. J. Simske, "Occluded image function: A novel measure for evaluating machine learning classifiers for biometrics," *Journal of Imaging Science and Technology*, vol. 66, no. 1, 2022.

[73] O. Ronneberger, P. Fischer, and T. Brox., "U-net: Convolutional networks for biomedical image segmentation," *Medical Image Computing and Computer-Assisted Intervention*, vol. 9351, p. 234–241, 2015.

[74] O. Çiçek, A. Abdulkadir, S. Lienkamp, and T. Brox, "3d u-net: Learning dense volumetric segmentation from sparse annotation," in *In Proceedings of the International Conference on Medical Image Computing and Computer-Assisted Intervention*, 2016.

[75] O. Oktay1, J. Schlemper, L. L. Folgoc, M. Lee, M. Heinrich, K. Misawa, K. Mori, S. McDonagh, N. Y. Hammerla, B. Kainz, B. Glocker, and D. Rueckert, "Attention u-net: Learning where to look for the pancreas," *arXiv:1804.03999v3 [cs.CV] 20 May 2018*, 2018.

[76] A. J. Clark, W. A. Gallus, and M. L. Weisman, "Neighborhood-based verification of precipitation forecasts from convection-allowing ncar wrf model simulations and the operational nam," *Weather and Forecasting*, vol. 25, no. 5, pp. 1495–1509, 2010.

[77] M. H. Rafiei and H. Adeli, "A new neural dynamic classification algorithm," *IEEE transactions on neural networks and learning systems*, vol. 28, no. 12, pp. 3074–3083, 2017.

[78] D. Pereira, M. Piteri, A. Souza, J. Papa, and H. Adeli, "Fema: A finite element machine for fast learning," *Neural Computing and Applications*, vol. 32, no. 10, 05 2020.

[79] K. M. R. Alam, N. Siddique, and H. Adeli, "A dynamic ensemble learning algorithm for neural networks," *Neural Computing and Applications*, vol. 32, no. 10, pp. 8675–8690, 2020.